Multifunctionality of Layered Materials

Septiany, Liany

DOI:
10.33612/diss.182500502

Chapter 4

Polar Structure and Two-Dimensional Antiferromagnetic Properties of Arylamine-based Manganese Chloride Layered Organic-Inorganic Perovskites

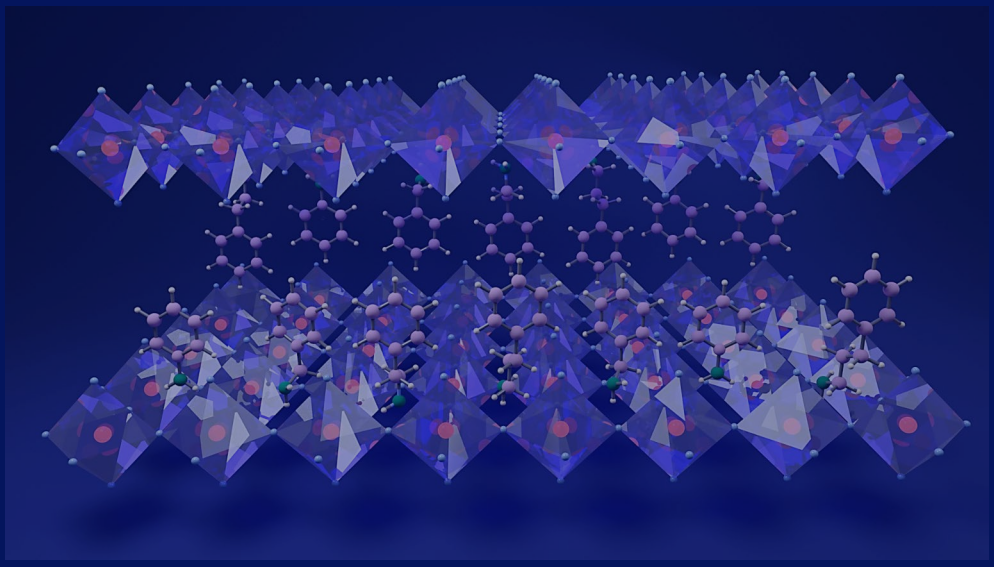

L. Septiany, D.Tulip, M. Chislov, J.Baas, G.R. Blake

Polar Structure and Two-Dimensional Antiferromagnetic Properties of Arylamine-based Manganese Chloride Layered Organic-Inorganic Perovskites. *Inorganic Chemistry*. **2021.** In Press

Abstract

Multiferroic properties, where ferroelectric and (anti)ferromagnetic order are found simultaneously in one material, are known for a small number of two-dimensional (2D) inorganic-organic hybrid perovskites. Here, we study a series of $MnCl_4$-based 2D perovskites with arylamine cations, namely $C_6H_5(C_xH_{2x})_2MnCl_4$ (x = 0,1,2,3), for which the x = 0, 1 and 3 members are reported for the first time. The compounds with x = 1, 2, and 3 adopt polar crystal structures to well above room temperature. We argue that the inversion symmetry breaking in these compounds is related to the rotational degree of freedom of the organic cations, which determine the hydrogen bonding pattern that links the organic and inorganic layers. We show that the buckling of $MnCl_6$ octahedra is not the primary mechanism involved in inversion symmetry breaking in these materials. All four compounds show 2D Heisenberg antiferromagnetic behaviour. A ferromagnetic component develops in each case below the long-range magnetic ordering temperature of ~42-46 K due to spin canting.

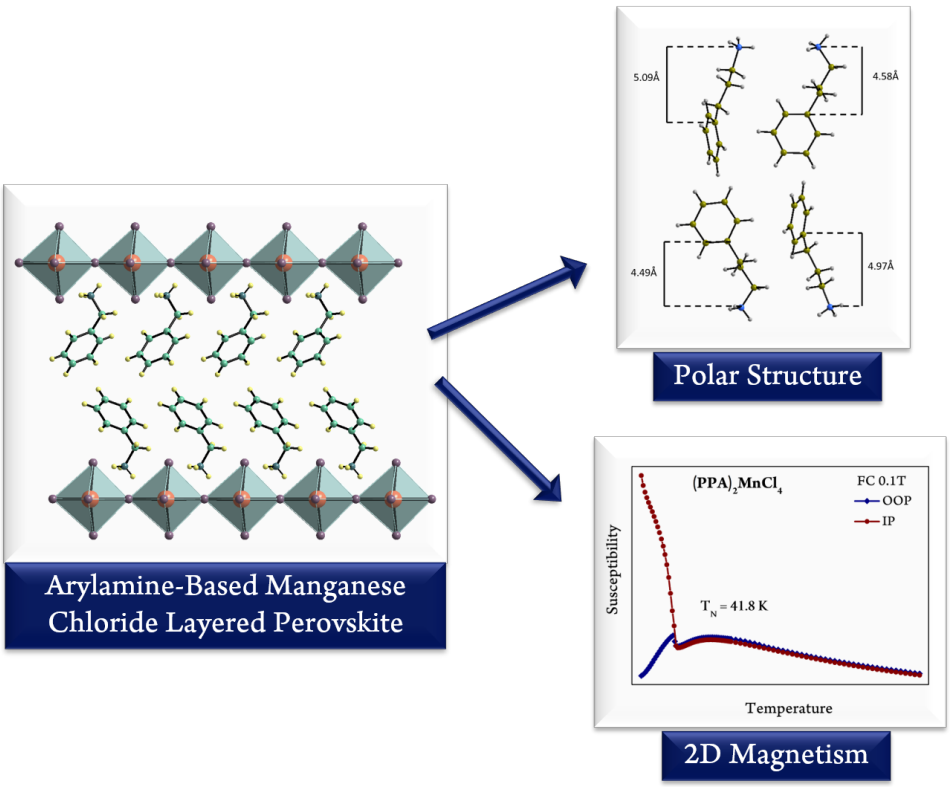

4.1 Introduction

Two-dimensional (2D) inorganic-organic halide perovskites containing lead and tin have in recent years been studied intensively in the context of their excellent photovoltaic and optoelectronic properties.[1–5] However, 2D perovskites that contain transition metals can also exhibit multiferroic properties where ferroelectricity coexists with magnetic order. Such materials open the prospect of manipulating magnetic order by an applied electric field, and controlling ferroelectric order by an applied magnetic field, which can potentially lead to improved electronic devices.[6–8]

For 2D halide perovskites it has been reported that arylamine-based organic cations, with flexible alkyl-ammonium tails compared to the rigid phenyl ring, can be used to introduce more distortion to the structure, sometimes resulting in a polar structure at room temperature. For example, $(C_6H_5C_2H_4NH_3)_2CuCl_4$ and $(C_6H_5C_4H_8NH_3)_2CuCl_4$ are reported to exhibit simultaneous polarization and magnetic ordering, giving multiferroic properties.[9,10] In the former it is thought that either a slight tilt of the organic cations breaks inversion symmetry, or that an order-disorder transition involving hydrogen bonding configurations is responsible. In the latter the mechanism is also thought to involve hydrogen bond ordering. However, there are as yet no conclusive guidelines as to which structural features lead to inversion symmetry breaking or to the mechanisms by which this can occur. The significance of inversion symmetry breaking is not limited to the field of multiferroic materials, but has important consequences for many other potential applications of inorganic-organic hybrid perovskites including their optoelectronic properties, as summarized in several recent reviews.[11–13] Therefore, there is a need to study more examples of polar layered inorganic-organic perovskites and to understand how and why inversion symmetry can be broken.

Compared to three-dimensional (3D) hybrid perovskites, 2D materials have better stability with respect to degradation and are more versatile with respect to the organic cations that can be incorporated. The structure generally consists of inorganic layers, usually in the form of corner-shared metal halide octahedra, which are separated by bilayers of the organic cation. The two blocks are connected by hydrogen bonding between the protons of the ammonium group and the halide anions. The corner-shared octahedral network in the inorganic layers is often distorted. The voids

between adjacent octahedra are occupied by the ammonium group of the organic cation, which may have different conformations related to the length of the alkyl tail. Layered perovskites are mostly reported to have centrosymmetric structures, but this might be due to the difficulty of assigning the correct space group. For example, Kamminga et al. found that $(C_6H_5C_2H_4NH_3)_2MnCl_4$ has a polar structure at room temperature after a detailed structural analysis, whereas the same compound was previously assigned to a centrosymmetric space group.[14] Here we present the structure of three novel $MnCl_4$-based layered perovskites, by which we show that with sufficient alkyl-ammonium tail length we can obtain a polar structure at room temperature.

Layered inorganic-organic perovskites are also known for their interesting magnetic properties. Since the metal halide layers are often separated by more than one nanometre, they tend to behave as quasi-two-dimensional Heisenberg magnets. Depending on the metal cations used in the inorganic layer, they can exhibit ferromagnetic ordering (Cu^{2+})[9,10,15–17] or antiferromagnetic ordering (Mn^{2+} and Fe^{2+}).[18–23] In previous studies, 2D $MnCl_4$-based perovskites were shown to undergo long-range antiferromagnetic ordering with ordering temperatures varying from ~39-47K.[18–21] Although an ideal two-dimensional Heisenberg magnet does not undergo ordering at any finite temperature,[24] it may still occur due to Ising anisotropy or the Dzyaloshinsky-Moriya (DM) interaction.[19] Lee et al. reported that the ordering temperature in 2D $MnCl_4$-based perovskites decreases with increasing length of the organic cations for straight alkylammonium chains (C1-C4) until a lowest value of ~43 K is reached,[19] due to a decrease in the interlayer exchange interaction as the distance increases. However, as the length of the cation increases beyond 8 carbon atoms, the superexchange interaction alone cannot describe the trend in transition temperature as the relative influence of Ising anisotropy and DM interactions become more pronounced. Park et al. reported canted antiferromagnetism for single crystals of $(C_6H_5C_2H_4NH_3)_2MnCl_4$, where the spin canting was observed in low applied magnetic field below the magnetic ordering temperature[18] and the magnetization showed significant anisotropy between the in-plane and out-of-plane directions. The easy-axis was claimed to lie along the layer stacking direction.

In this study we discuss the effect of organic cation length on the breaking of inversion symmetry and on the magnetic properties of 2D $MnCl_4$-based perovskites. We use four different arylamine based organic cations, namely phenylamine (aniline, $C_6H_5NH_3$), phenylmethylamine

(benzylamine, $C_6H_5CH_2NH_3$), phenylethylamine (phenethylamine, $C_6H_5C_2H_4NH_3$) and phenylpropylamine ($C_6H_5C_3H_6NH_3$). We find that only $(C_6H_5NH_3)_2MnCl_4$ crystallizes in a centrosymmetric structure, while the others adopt polar structures from 100 K to above room temperature. All the compounds show two-dimensional antiferromagnetism with transitions to a canted, long-range ordered state below ~42-46K.

4.2 Experimental Details

4.2.1 Crystal Growth

Aniline hydrochloride (Sigma Aldrich; 97%), benzylamine (Sigma Aldrich, 99%), 2-phenethylamine hydrochloride (Sigma Aldrich; ≥98%) and 3-phenyl-1-propylamine (Sigma Aldrich; 98%) were used as the arylammonium source. Salts of phenylmethylammonium and phenylpropylammonium chloride were synthesized by mixing the organic liquid with HCl (Sigma Aldrich; 2.5M in EtOH) in ethanol absolute, resulting in a white powder. The powder was then washed with diethylether (Macron Chemicals) and vacuum dried overnight.

A 1:2 molar ratio of $MnCl_2$ (Sigma Aldrich; ≥ 99%) and the respective arylammonium chloride salt was dissolved in absolute ethanol. Single crystals were grown by slow evaporation of the solvent at 60˚C. After ~1 week, single crystals were obtained from solution as platelets with different colours depending on the organic cation used.

4.2.2 X-Ray Diffraction

Single-crystal X-ray diffraction (XRD) measurements were carried out using a Bruker D8 Venture diffractometer operating with Mo-Kα radiation, equipped with a Photon 100 area detector and a Triumph monochromator. The crystals were placed on a glass fibre using a commercial acrylate glue for measurements above room temperature, while for low temperature measurement the crystals were mounted on a nylon fibre loop using cryo-oil. An Oxford Cryostream Plus with dry nitrogen flow was used to regulate the measurement temperature. The data obtained were processed by the Bruker APEX III software. The structures were solved by direct methods and refinement was carried out using the SHELX97 software[25].

Furthermore, the crystals were hand-ground into a fine powder using an agate mortar and pestle for powder XRD measurement at room temperature. The measurements were carried out using a Bruker D8 Advance diffractometer equipped with a Cu-Kα source. The structural parameters were determined by Rietveld refinement using the GSAS software.[26]

4.2.3 Magnetic Measurement.

Magnetic measurements were carried out using a Quantum Design MPMS SQUID magnetometer. The single crystals, all in the form of platelets, were measured with the applied field along the in-plane and out-of-plane orientations. The temperature dependence of the DC magnetization was measured on warming from 5-300 K after field cooling in 1000 Oe. Measurements of magnetization versus applied field were carried out up to 6 T at different temperatures, after cooling in zero magnetic field.

4.3 Results and Discussion

4.3.1 Structural Analysis

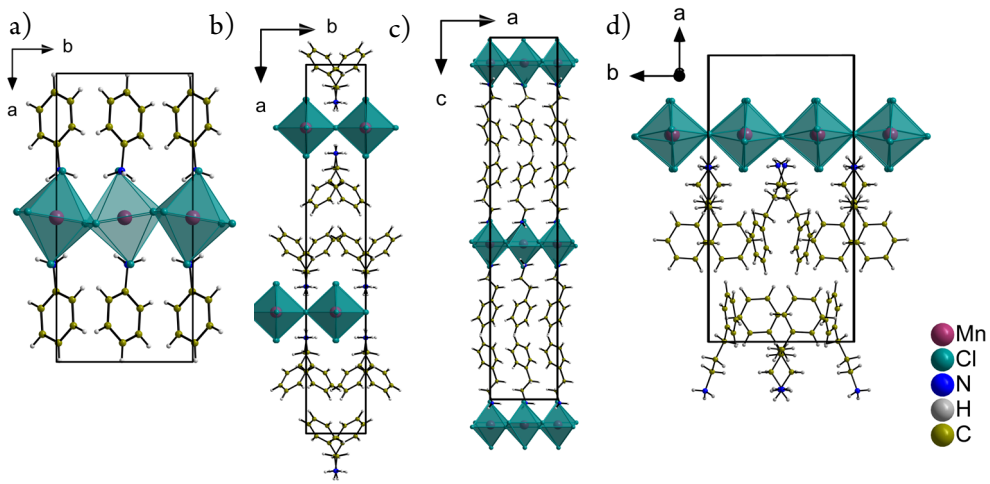

Figure 4.1 *Crystal structures of a) $(PA)_2MnCl_4$, b) $(PMA)_2MnCl_4$, c) $(PEA)2MnCl_4$ and d) $(PPA)_2MnCl_4$ at 100 K.*

Table 4.1 Structural parameters of $(PA)_2MnCl_4$, $(PMA)_2MnCl_4$, $(PEA)_2MnCl_4$, and $(PPA)_2MnCl_4$ at 100K.

	$(PA)_2MnCl_4$	$(PMA)_2MnCl_4$	$(PEA)_2MnCl_4$	$(PPA)_2MnCl_4$
Organic cation	$(C_6H_5NH_3)$	$(C_6H_5CH_2NH_3)$	$(C_6H_5CH_2CH_2NH_3)$	$(C_6H_5CH_2CH_2CH_2NH_3)$
Molecular Weight	385.01 g/mol	413.07 g/mol	441.12 g/mol	469.18 g/mol
Space group	$P2_1/c$ Centrosymmetric	Cc Polar	$Pca2_1$ Polar	Pc Polar
a (Å)	15.3747(11)	32.496(5)	7.2352(10)	20.6463(21)
b (Å)	7.1706(5)	5.1630(8)	7.1390(10)	10.3297(11)
c (Å)	7.1112(5)	10.3195(14)	39.028(6)	10.3353(10)
β (°)	99.543(3)	98.139(4)	90.000	98.783(5)
V (Å³)	773.13(9)	1715.1(4)	2015.9(5)	2178.3(4)
Z	2	4	4	4
density (g/cm³)	1.654	1.599	1.453	1.431
goodness of fit	0.7945	1.1453	1.249	1.047
R1	0.0404	0.0893	0.0852	0.1060
largest diff peak/hole (e/Å³)	0.47/-0.39	1.30/-0.93	1.77/-1.89	2.12/-1.07
Mn-Cl bond distances	2.5749(1) (eq)	2.586(2) (eq)	2.518(4) (eq)	1st octahedron
	2.5727(5) (eq)	2.585(2) (eq)	2.698(4) (eq)	2.586(2) (eq)
	2.4655(2) (ax)	2.538(3) (eq)	2.513(4) (eq)	2.585(2) (eq)
		2.627(3) (eq)	2.613(4) (eq)	2.604(4) (eq)
		2.474(3) (ax)	2.493(8) (ax)	2.643(4) (eq)
		2.478(3) (ax)	2.483(7) (ax)	2.454(4) (ax)
				2.478(4) (ax)
				2nd octahedron
				2.577(2) (eq)
				2.589(2) (eq)
				2.627(4) (eq)
				2.617(4) (eq)
				2.439(4) (ax)
				2.492(4) (ax)
Mn-Cl-Mn bond angles	157.578(19)	178.55(14)	164.22(15)	162.58(15)
		173.59(9)	165.70(16)	158.98(15)
				177.93(8)
				174.66(9)

The crystal structures of $(C_6H_5NH_3)_2MnCl_4$ ($(PA)_2MnCl_4$/**1**), $(C_6H_5CH_2NH_3)_2MnCl_4$ ($(PMA)_2MnCl_4$/**2**) and $(C_6H_5CH_2CH_2CH_2NH_3)_2MnCl_4$ ($(PPA)_2MnCl_4$/**4**) have not previously been reported, whereas the n=2 compound $(C_6H_5CH_2CH_2NH_3)_2MnCl_4$ ($(PEA)_2MnCl_4$/**3**) has been studied previously;[14] the structure of our current crystals of **3** is consistent with the earlier report. The structures of **1**-**4** determined at 100 K are presented in Fig. 4.1a-d. Compound **1** crystallizes in a centrosymmetric (non-polar) space group whereas **2**, **3**, and **4** have polar structures. The structural parameters are listed in Table 4.1.

We observe the breaking of inversion symmetry when the organic cation has an alkyl chain of at least one carbon atom. To compare, $MnCl_4$-based layered hybrid perovskites adopt a centrosymmetric structure when the cation has a simple alkyl chain.[27–30] This implies that the introduction of a phenyl ring leads to a polar structure. It is therefore useful to examine the structures of **1**-**4** in more detail to identify the mechanism by which inversion symmetry is broken.

It was previously reported that the onset of a polar phase for **3** involves the opening of a small dihedral angle between the phenyl rings of adjacent PEA molecules, which are crystallographically distinct.[14] The rotation of the phenyl rings also induces a change in the bond angles and hence lengths of the alkyl ammonium tails of the PEA molecules. This difference gives rise to an asymmetric approach of the organic cations to the inorganic layer, inducing different hydrogen bond lengths associated with the two molecules, which also shifts the Mn^{2+} away from the centre of the octahedron. With increasing number of carbon atoms in the alkyl-ammonium tail of the organic cation, there are fewer symmetry operations relating equivalent organic molecules in the structure. Thus, compound **1** has only a single crystallographically distinct organic molecule, whereas **2** and **3** have two distinct molecules, and **4** has four different molecules. The alkyl ammonium tails of inequivalent molecules exhibit differences in length for compounds **2**, **3** and **4**, as depicted in Fig. 4.2.

This results in displacement of the molecules to different extents along the layer stacking axis, which likely occurs in order to accommodate close packing and beneficial van der Waals and/or electrostatic interactions between adjacent molecules in the double layer. It also reflects the more flexible conformation of alkyl chains compared to the rigid phenyl ring. The asymmetric approach

of inequivalent organic molecules to the inorganic layer also results in different hydrogen bonding patterns, which are shown in Fig. 4.3. To retain effective hydrogen bond lengths between N—H----Cl—Mn, the six Mn-Cl bonds in an octahedron become unequal in **2**, **3** and **4**, thus the $MnCl_6$ octahedra are no longer perfectly regular (see table 4.1). Furthermore, the in-plane Mn-Cl-Mn bond angles linking adjacent MCl_6 octahedra also deviate from 180°. However, this buckling of the octahedra is not only observed in the polar structures of **2**, **3** and **4**, but is also present in **1**. For **1**, effective hydrogen bonding can again only be preserved while simultaneously accommodating van der Waals interactions between the adjacent molecules in the double layer when the Mn^{2+} and Cl^- ions are slightly displaced, giving rise to buckling. This observation supports the notion that the polar structure of $MnCl_4$-based layered perovskites is not directly related to the buckling of the octahedra. For comparison, Table 4.2 shows the buckling angles of centrosymmetric $(CH_3NH_3)_2MnCl_4$ ($(MA)_2MnCl_4$) and $(C_2H_5NH_3)_2MnCl_4$ ($(EA)_2MnCl_4$) in addition to **1**-**4**. The buckling angle is defined as the angle between the line connecting the two apical chloride ions of an octahedron and the long unit cell axis. In all cases, the buckling and hydrogen bonding lead to shifts of Mn^{2+} from the middle of the octahedra, which cancel for the centrosymmetric compounds. The off-centre shift of the Mn^{2+} ion is calculated by taking the weighted average of the 6 Cl^- as the centre of the octahedron, and subtracting the value to the apical bond length to obtain the shift along the long axis. The magnitudes of these shifts are also listed in Table 4.2, together with the Glazer octahedral tilt system, for which we regard the stacking axis as c for the purposes of the notation. We note that a phase transition involving the appearance of octahedral buckling leads to ferroelectric order in $(PEA)_2CuCl_4$[9] via the onset of hydrogen bond order associated with rotation of the terminal NH_3 group of the PEA cation. However, this appears to be an exception to the rule followed by **2**-**4**, where buckling of the metal halide octahedra is not the primary mechanism that breaks inversion symmetry.

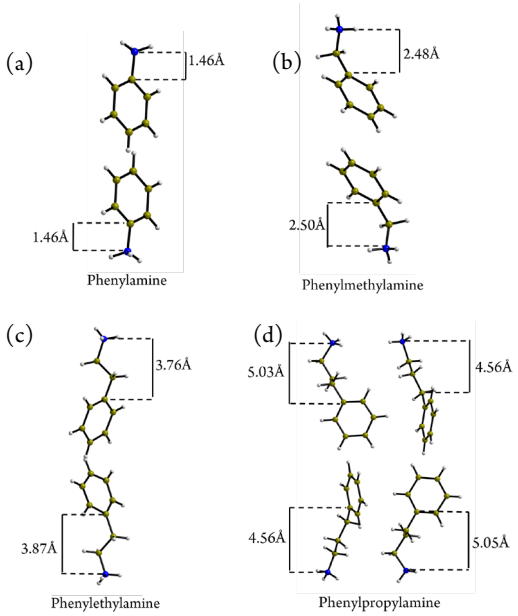

Figure 4.2 *Length of alkyl-ammonium tails in adjacent organic cations in* ***1****-****4****.*

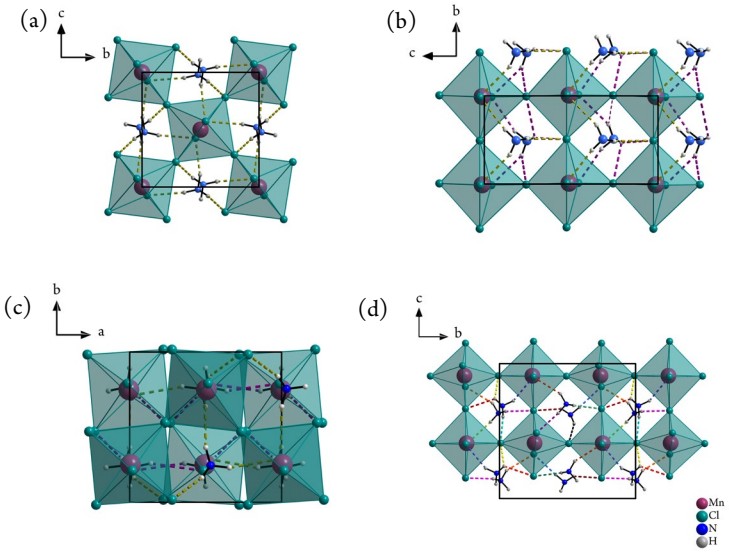

Figure 4.3 *Hydrogen bonding patterns in a) $(PA)_2MnCl_4$, b) $(PMA)_2MnCl_4$, c) $(PEA)_2MnCl_4$, and d) $(PPA)_2MnCl_4$. Dashed lines with different colours indicate hydrogen bonds from crystallographically distinct NH_3-groups.*

Table 4.2 Buckling angle and Mn^{2+} off-centre shifts for $MnCl_4$-based layered perovskites

Compound	Space group	Buckling angle (°)	Mn^{2+} shift (pm)	Glazer tilt system
$(MA)_2MnCl_4$[30,31]	$P4_2/ncm$	7.42	4.0	$a^+a^+c^-$
$(EA)_2MnCl_4$[30,32]	Pbca	7.13	6.7	$a^-a^-c^0$
$(PA)_2MnCl_4$	$P2_1/c$	13.99	7.2	$a^-b^-c^0$
$(PMA)_2MnCl_4$	Cc	7.78	7.2	a^+b^-c
$(PEA)_2MnCl_4$	$Pca2_1$	6.8	5.0	$a^-b^-c^0$
$(PPA)_2MnCl_4$	Pc	2.7 19.1	9.2 9.1	$a^-b^-c^0$

Single-crystal XRD shows that the centrosymmetric $P2_1/c$ structure of **1** is retained from 100 K up to at least 370 K, and the polar Cc structure of **2** is retained up to at least 400 K (see Appendix A, Table 4.5). No significant changes in the structures of **1** and **2** occur in this temperature range, other than an increase in the lattice parameters due to thermal expansion. This is also supported by room temperature powder XRD, the profiles of which were fitted reasonably well using the structural parameters obtained from single-crystal XRD (see Appendix, Fig. 4.7). In contrast, **3** undergoes two successive phase transitions above 100 K, first to a polar orthorhombic Aea2 phase at 363 K in which the organic cations become partially disordered and the buckling of the octahedral is removed, and then to a centrosymmetric tetragonal I4/mmm phase at 423 K (the decomposition temperature is ~470 K) in which the cations are fully rotationally disordered.[14] In the case of **4**, the atomic coordinates determined by single-crystal XRD at 100 K were used to fit the powder XRD pattern in Fig. 4.7, and the fit suggests that no phase transition occurs below room temperature. Differential scanning calorimetry (DSC)- Thermal gravimetric (TG) measurements were performed on **1**, **2** and **4** from 100-500 K, and provided no evidence for any phase transitions below the decomposition temperatures of ~380 K, ~440 K and ~430 K, respectively (see Appendix, Fig. 4.8 and 4.9).

Inversion symmetry breaking has been reported in several other 2D perovskites with cations containing phenyl or cycloalkane rings. For example, $(PMA)_2PbCl_4$[33] adopts a high-temperature non-polar (*Cmca*) state in which the organic cation exhibits two-fold orientational disorder, and with decreasing temperature a polar transition occurs, below which only one of the two orientations is preserved (space group $Cmc2_1$). The same mechanism has been reported for a fluorinated phenyl

ring in $(2FPMA)_2PbCl_4$ (*I4/mmm* to *Cmc2₁* transition),[34] and for cycloalkane cations in $(CHA)_2PbBr_{4-x}I_x$ (CHA=cyclohexylammonium, *Cmca* to *Cmc2₁* transition)[35] and $(CPA)_2CdBr_4$ (CPA=cyclopentylammonium, *Pnam* to *Pna2₁* transition).[36] Polar structures have further been reported for $(PEA)_2SnI_4$ (space group *P1*),[37] $(PMA)_2PbBr_4$ (space group *Cmc2₁*),[38] and $(PEA)_2GeI_4$ (space group *P1*),[39] which might arise from the same structural considerations. A rotational order-disorder phase transition has also been reported for the simple butylammonium (C4A) cation in $(C4A)_2PbCl_4$ (*Cmca* to *Cmc2₁*),[40] and $(C5A)_2CuCl_4$ is reported to be polar (C5A=pentylammonium, space group *Cc*).[41]

4.3.2 Two-dimensional Magnetism

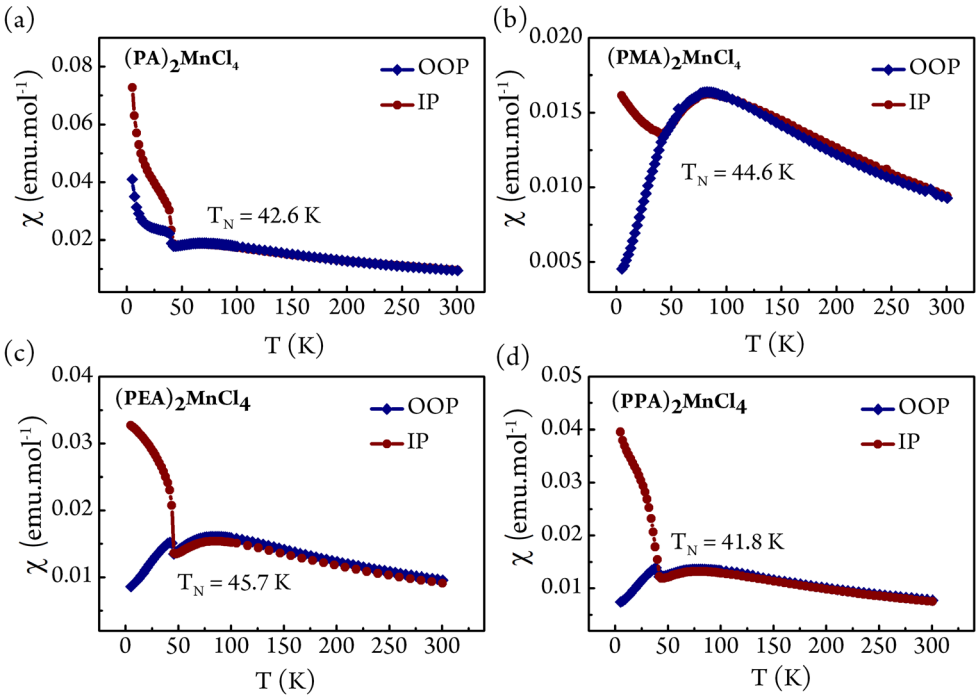

Figure 4.4 *Magnetic susceptibility versus temperature for compounds* ***1*** *to* ***4*** *measured with a field of 1000 Oe applied along the in-plane (IP) and out-of-plane (OOP) directions*

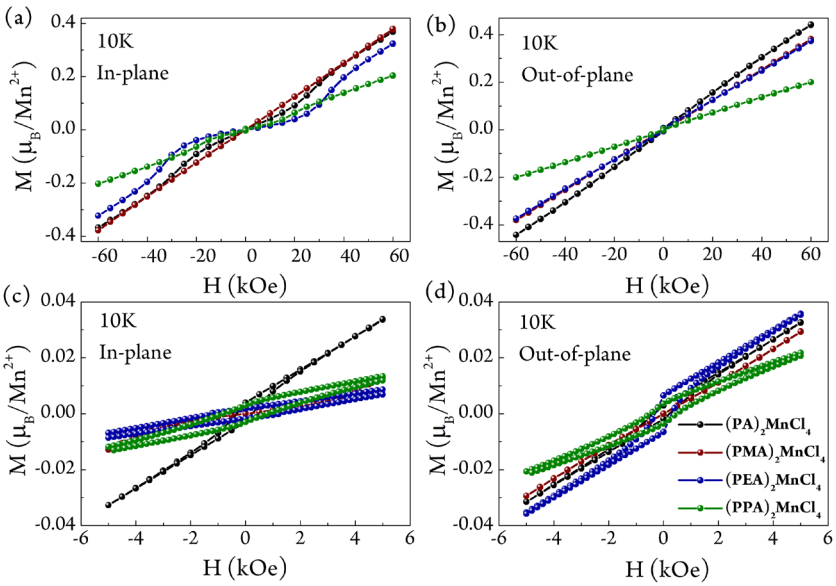

Figure 4.5 *Field-dependent magnetization measured at 10 K at high and low magnetic field along the a,c) in-plane and b,d) out-of-plane direction*

Compounds **1** to **4** all show two-dimensional antiferromagnetic characteristics, with a broad maximum in the magnetic susceptibility versus temperature curve at ~70-80K (Fig. 4.4). For each compound a sharp change in slope takes place in the range 42 – 46 K, suggesting the onset of three-dimensional order. Compound **1** shows a slightly higher susceptibility below the 3D ordering temperature (T_N) when the field is applied in-plane compared to out-of-plane, but the overall behaviour is similar. In contrast, for compounds **2**, **3** and **4**, the susceptibility drops and approaches zero with decreasing temperature when measured out-of-plane, suggesting that the easy-axis lies in this direction. The susceptibility rises steeply when measured parallel to the inorganic layer, suggesting a spontaneous magnetization as described in previous reports.[18] An ideal 2D Heisenberg antiferromagnet should not have a finite ordering temperature; however, in real magnetic systems, we cannot ignore weak exchange interactions in the perpendicular direction, as well as Ising anisotropy and/or Dzyaloshinski-Moriya (DM) interactions, all of which can lead to 3D ordering. It is known that the spins in 2D manganese halide perovskites are aligned in antiparallel fashion in-plane, and the weak ferromagnetism arises due to spin canting as a result of antisymmetric DM interactions associated with the tilted $MnCl_6$ octahedra.[19]

We observe that beside the anisotropy at low temperature, the in-plane and out-of-plane susceptibility curves from ~100-300K almost perfectly lie on top of each other as expected for two-dimensional magnets (see Fig. 4.4). Curie-Weiss fits to the inverse susceptibility data were performed in the range 150-300 K, and the extracted Weiss constants (θ) and effective magnetic moments (μ_{eff}) are given in Table 4.3. The Weiss constants are large and negative for all four compounds, confirming strong antiferromagnetic interactions. The effective moments are in the range 5.5-5.9 μ_B/Mn^{2+}, which is consistent with the expected value of 5.92 μ_B for the high-spin configuration of the Mn^{2+} ion.

Field-dependent magnetization measurements were carried out to probe the weak ferromagnetism below the ordering temperature. As depicted in Fig. 4.5, narrow hysteresis loops are apparent for **1**, **3** and **4** when the applied field is in-plane. The magnetization then increases linearly at higher fields, consistent with the dominant antiferromagnetic component. The coercive field and remanent magnetization of the compounds are listed in Table 4.3, together with the spin canting angle α obtained from the relation $\sin \alpha = M_R/Ms$.

For the out-of-plane magnetization, we observe inflection points that might be related to a spin-flop transition as previously observed for **3**.[19] Spin-flop transitions in an antiferromagnet occur when a magnetic field perpendicular to the easy-axis causes the antiparallel spins to flop to the perpendicular direction. This critical magnetic field is known as the spin-flop field (H_{sf}),[42] which is also listed in Table 4.3.

Table 4.3 Magnetic parameters of 1 to 4

Compound	T_N (K)	θ (K)	μ_{eff} (μ_B)	H_{sf} (kOe)	$H_{Coercive}$ (Oe)	M_R (μ_B)	α (deg.)
$(PA)_2MnCl_4$	42.6	-126	5.75	30	240	0.0036	0.036
$(PMA)_2MnCl_4$	44.6	-135	5.71	10	-	-	-
$(PEA)_2MnCl_4$	45.7	-162	5.96	35	280	0.0033	0.032
$(PPA)_2MnCl4$	41.8	-148	5.53	20	490	0.0028	0.029

We analyzed the two-dimensional Heisenberg antiferromagnetism based on Curély's work on square lattice antiferromagnets.[24,43–45] The equation below can be used to explain the temperature dependent magnetic susceptibility of two-dimensional antiferromagnets and is known to work well for the Mn^{2+} ion:

$$\chi = \frac{\beta G^2}{3}\left(\frac{1+L(-\beta J)}{1-L(-\beta J)}\right)^2 \quad (4.1)$$

Here L, G, and J are the Langevin function, Landé factor and the exchange energy, respectively, and $\beta = 1/kT$ (k is the Boltzmann constant). Fig. 4.6 shows corresponding fits to the susceptibility of **1**-**4**. Curély also derived another equation that allows us to estimate the theoretical temperature of maximum susceptibility, referred to as $T(\chi_{max})_{Th}$, given by

$$\frac{kT(\chi max)}{JS(S+1)} = 1.2625 \quad (4.2)$$

Here S = 5/2 for Mn^{2+}. Table 4.4 shows the Landé factor (G), exchange energy (J), and both the theoretical and experimental values of $T(\chi_{max})$.

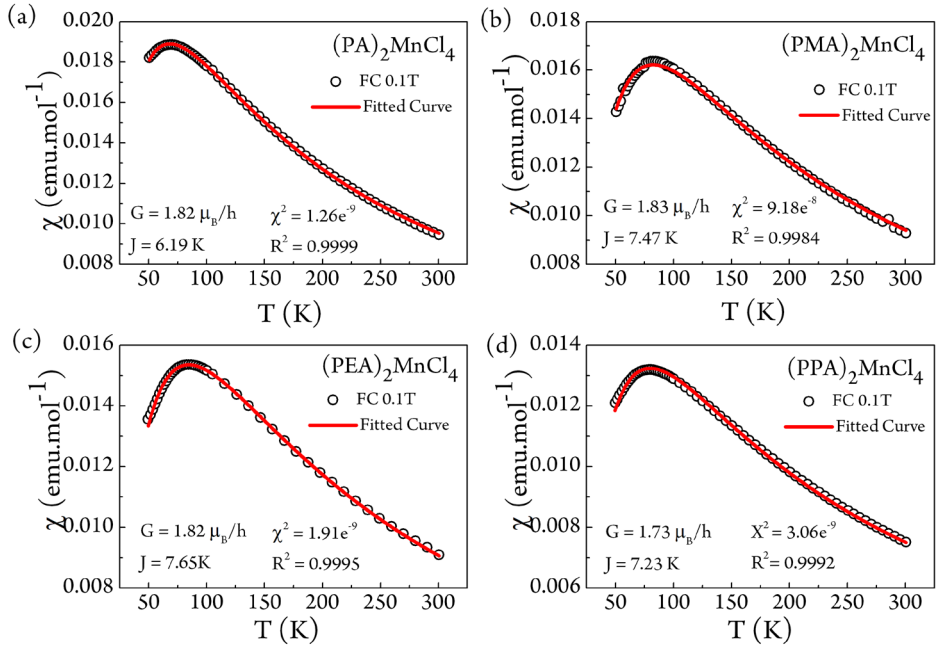

Figure 4.6 *Temperature dependent magnetic susceptibility along the in-plane direction of* ***1***-***4*** *fitted (red line) using Eq. (4.1)*

Table 4.4 Landé factor, exchange energy and temperature at χ_{max}

Compound	G	J/k_B	$T(\chi_{max})_{Th}$	$T(\chi_{max})_{Exp}$	$\Delta T(\chi_{max})_{th} / T(\chi_{max})_{th}$
$(PA)_2MnCl_4$	1.82 $\mu_B/\hbar$	6.19 K	68.4 K	68.4 ± 2 K	0 %
$(PMA)_2MnCl_4$	1.83 $\mu_B/\hbar$	7.47 K	82.5 K	82.3 ± 2 K	0.24%
$(PEA)_2MnCl_4$	1.82 $\mu_B/\hbar$	7.65 K	85.4 K	84.3 ± 2 K	1.3%
$(PPA)_2MnCl_4$	1.73 $\mu_B/\hbar$	7.23 K	79.9 K	78.8 ± 2 K	1.4%

Equations (4.1) and (4.2) have previously been used to explain the two-dimensional antiferromagnetic characteristics of $(MA)_2MnCl_4$ and other $MnCl_4$-based layered perovskites with linear alkyl chains.[19,24] Here, we show that layered perovskites with arylamine-based ligands also retain similar two-dimensional antiferromagnetic characteristics. The Landé factors are comparable to that of $(MA)_2MnCl_4$, reported as 1.89.[24] The temperatures of the maximum in susceptibility ($T(\chi_{max})$) calculated using Eq. (4.2) are comparable with those obtained experimentally (Table 4.4), showing that all four compounds exhibit 2D-Heisenberg antiferromagnetic behavior above the Néel temperature.

4.4 Conclusions

We report three new $MnCl_4$-based layered inorganic-organic perovskite compounds with the arylamine-based organic cations PA, PMA and PPA, and we compare their properties with the previously studied analogue containing the PEA cation. We show that the presence of an alkyl tail of at least one carbon atom is important to obtain a polar crystal structure. We suggest that the rotational degree of freedom of such organic cations is an important factor that can give rise to the breaking of inversion symmetry. To achieve beneficial van der Waals and/or electrostatic interactions, adjacent organic molecules arrange themselves such that the flexible alkyl tails have different lengths when approaching the inorganic layer. This gives rise to different hydrogen bonding patterns between the organic and inorganic layer, which also results in buckled MCl_6 octahedra. The buckling of the MCl_6 octahedra does not itself govern the presence of a polar structure. For $(PMA)_2MnCl_4$ and $(PPA)_2MnCl_4$ the polar structure is stable up to the decomposition temperature. We observe two-dimensional antiferromagnetism in all four compounds, manifested by a broad maximum in the magnetic susceptibility in the range ~70-80 K that can be fitted by the 2D Heisenberg model of Curély. All samples show the presence of a weak ferromagnetic component below the long-range ordering temperature of 42-46 K due to spin canting. The presence of polar structures suggests the possibility of ferroelectric ordering, which when combined with the canted antiferromagnetic ordering leads to the prospect of multiferroic properties.

4.5 References

1 G. Grancini and M. K. Nazeeruddin, *Nat. Rev. Mater.*, 2019, **4**, 4–22.

2 C. C. Stoumpos, C. D. Malliakas and M. G. Kanatzidis, *Inorg. Chem.*, 2013, **52**, 9019–9038.

3 H. Wang, C. Fang, H. Luo and D. Li, *J. Semicond.*, 2019, **40**, 041901.

4 L. Pedesseau, D. Sapori, B. Traore, R. Robles, H. H. Fang, M. A. Loi, H. Tsai, W. Nie, J. C. Blancon, A. Neukirch, S. Tretiak, A. D. Mohite, C. Katan, J. Even and M. Kepenekian, *ACS Nano*, 2016, **10**, 9776–9786.

5 Z. Cheng and J. Lin, *CrystEngComm*, 2010, **12**, 2646–2662.

6 N. A. Spaldin and R. Ramesh, *Nat. Mater.*, 2019, **18**, 203–212.

7 W. Eerenstein, N. D. Mathur and J. F. Scott, *Nature*, 2006, **442**, 759–765.

8 D. Khomskii, *Physics*, 2009, **2**, 20.

9 A. O. Polyakov, A. H. Arkenbout, J. Baas, G. R. Blake, A. Meetsma, A. Caretta, P. H. M. Van Loosdrecht and T. T. M. Palstra, *Chem. Mater.*, 2012, 24, 133–139.

10 B. Huang, B. Y. Wang, Z. Y. Du, W. Xue, W. J. Xu, Y. J. Su, W. X. Zhang, M. H. Zeng and X. M. Chen, *J. Mater. Chem. C*, 2016, **4**, 8704–8710.

11 S. Shahrokhi, W. Gao, Y. Wang, P. R. Anandan, M. Z. Rahaman, S. Singh, D. Wang, C. Cazorla, G. Yuan, J. M. Liu and T. Wu, *Small Methods*, 2020, **4**, 2000149.

12 R. Pandey, G. Vats, J. Yun, C. R. Bowen, A. W. Y. Ho-Baillie and J. Seidel, 2017, *arXiv:1705.05529*.

13 P. Nandi, D. Topwal, N.-G. Park and H. Shin, *J. Phys. D. Appl. Phys.*, 2020, **53**, 493002.

14 M. E. Kamminga, R. Hidayat, J. Baas, G. R. Blake and T. T. M. Palstra, *APL Mater.*, 2018, **6**, 066106.

15 R. D. Willett, C. J. Gómez-García and B. Twamley, *Eur. J. Inorg. Chem.*, 2012, **4**, 3342–3348.

16 A. Dupas, K. Le Dang, J. P. Renard and P. Veillet, *J. Chem. Phys.*, 1976, **65**, 3–7.

17 B. Huang, J. Y. Zhang, R. K. Huang, M. K. Chen, W. Xue, W. X. Zhang, M. H. Zeng and X. M. Chen, *Chem. Sci.*, 2018, **9**, 7413–7418.

18 S.-H. Park, I.-H. Oh, S. Park, Y. Park, J. H. Kim and Y.-D. Huh, *Dalt. Trans.*, 2012, **41**, 1237–1242.

19 K. W. Lee, C. H. Lee, C. E. Lee and J. Kang, *Phys. Rev. B - Condens. Matter Mater. Phys.*, 2000, **62**, 95–98.

20 G. Heger, E. Henrich and B. Kanellakopulos, *Solid State Commun.*, 1973, **12**, 1157–1165.

21 W. D. van Amstel and L. J. de Jongh, *Solid State Commun.*, 1972, **11**, 1423–1429.

22 T. Nakajima, H. Yamauchi, T. Goto, M. Yoshizawa, T. Suzuki and T. Fujimura, *J. Magn. Magn. Mater.*, 1983, **31**–**34**, 1189–1190.

23 J. Han, S. Nishihara, K. Inoue and M. Kurmoo, *Inorg. Chem.*, 2015, **54**, 2866–2874.

24 J. Curély and J. Rouch, *Phys. B Condens. Matter*, 1998, **254**, 298–321.

25 G. M. Sheldrick, Acta Crystallogr. A, 2008, **64**, 112–122.

26 B. H. Toby, *J. Appl. Crystallogr.*, 2001, **34**, 210–213.

27 G. Heger, D. Mullen and K. Knorr, *Phys. Stat. Sol A*, 1975, **31**, 455-462.

28 T. Sakami, T. Ohtani, Y. Matsumoto, D. Ochi, X. Xi, S. Kamikawa, J. Ohyama, I. Ishii and T. Suzuki,

Solid State Commun., 2019, **290**, 49–54.

29 H. Arend, R. Hofmann and F. Waldner, *Solid State Commun.*, 1973, **13**, 1629–1632.

30 W. Depmeier, J. Felsche and G. Wildermuth, *J. Solid State Chem.*, 1977, **21**, 57–65.

31 K. S. Aleksandrov and J. Bartolome, *J. Phys. Condens. Matter*, 1994, **6**, 8219–8235.

32 I. H. Brunskill and W. Depmeier, *Acta Crystallogr. A*, 1982, **38**, 132–137.

33 W. Q. Liao, Y. Zhang, C. L. Hu, J. G. Mao, H. Y. Ye, P. F. Li, S. D. Huang and R. G. Xiong, *Nat. Commun.*, 2015, **6**, 7338.

34 P. P. Shi, S. Q. Lu, X. J. Song, X. G. Chen, W. Q. Liao, P. F. Li, Y. Y. Tang and R. G. Xiong, *J. Am. Chem. Soc.*, 2019, **141**, 18334–18340.

35 H. Y. Ye, W. Q. Liao, C. L. Hu, Y. Zhang, Y. M. You, J. G. Mao, P. F. Li and R. G. Xiong, *Adv. Mater.*, 2016, **28**, 2579–2586.

36 C. R. Huang, X. Luo, W. Q. Liao, Y. Y. Tang and R. G. Xiong, *Inorg. Chem.*, 2020, **59**, 829–836.

37 Y. Gao, Z. Wei, P. Yoo, E. Shi, M. Zeller, C. Zhu, P. Liao and L. Dou, *J. Am. Chem. Soc.*, 2019, **141**, 15577–15585.

38 K. Z. Du, Q. Tu, X. Zhang, Q. Han, J. Liu, S. Zauscher and D. B. Mitzi, *Inorg. Chem.*, 2017, **56**, 9291–9302.

39 P. Cheng, T. Wu, J. Zhang, Y. Li, J. Liu, L. Jiang, X. Mao, R. F. Lu, W. Q. Deng and K. Han, *J. Phys. Chem. Lett.*, 2017, **8**, 4402–4406.

40 C. Ji, S. Wang, L. Li, Z. Sun, M. Hong and J. Luo, *Adv. Funct. Mater.*, 2019, **29**, 2–7.

41 R. Willett, H. Place and M. Middleton, *J. Am. Chem. Soc.*, 1988, **110**, 8639–8650.

42 C. Bi, Y. Shao, Y. Yuan, Z. Xiao, C. Wang, Y. Gao and J. Huang, *J. Mater. Chem. A*, 2014, **2**, 18508–18514.

43 J. Curély, *Phys. B Condens. Matter*, 1998, **245**, 263–276.

44 J. Curély, *Phys. B Condens. Matter*, 1998, **254**, 277–297.

45 J. Curély and J. Kliava, *Phys. Status Solidi C*, 2014, **11**, 989–994.

APPENDIX

Table 4.5 Structural parameters of $(PA)_2MnCl_4$ at 100, 300 and 370K. There is no indication of any structural phase transition to a different space group.

	$(PA)_2MnCl_4$	$(PA)_2MnCl_4$	$(PA)_2MnCl_4$
Temp (K)	100	300	370
Space group	$P2_1/c$ Centrosymmetric	$P2_1/c$ Centrosymmetric	$P2_1/c$ Centrosymmetric
a (Å)	15.3747(11)	15.4983(15)	15.5910(4)
b (Å)	7.1706(5)	7.2403(6)	7.2858(17)
c (Å)	7.1112(5)	7.1788(6)	7.1848(16)
β (°)	99.543(3)	100.074(4)	100.606(8)
V (Å³)	773.13(9)	793.13(12)	802.2(3)
Z	2	2	2
density (g/cm³)	1.654	1.6121	1.5271
goodness of fit	0.7945	1.166	0.993
R1	0.0404	0.0422	0.0544
largest diff peak/hole (e/Å³)	0.47/-0.39	0.67/-0.72	0.79/-0.47
Mn-Cl bond length (Å)	2.5749(1) (eq)	2.5875(5) (eq)	2.5596(7)
	2.5727(1) (eq)	2.5946(5) (eq)	2.5910(7)
	2.4655(2) (ax)	2.4957(5) (eq)	2.4611(8)
Mn-Cl-Mn angle (degrees)	157.58(2)	159.33(2)	160.58(2)

Table 4.6 Structural parameters of $(PMA)_2MnCl_4$ at 100, 300 and 400K. There is no indication of any structural phase transition to different space group.

	$(PMA)_2MnCl_4$	$(PMA)_2MnCl_4$	$(PMA)_2MnCl_4$
Temp (K)	100	300	400
Space group	Cc Polar	Cc Polar	Cc Polar
a (Å)	32.4103(3)	32.939(4)	33.062(7)
b (Å)	5.1589(4)	5.1840(8)	5.1991(11)
c (Å)	10.2953(1)	10.4279(14)	10.486(2)
β (°)	98.139(4)	98.780(7)	98.542(1)
V (Å^3)	1704.05(3)	1759.8(4)	1782.4 (6)
Z	4	4	4
density (g/cm^3)	1.501	1.4829	1.5392
goodness of fit	1.125	1.500	1.310
R1	0.0868	0.0906	0.0756
largest diff peak/hole (e/Å^3)	1.88/-0.62	0.77/-1.23	1.81/-0.72
Mn-Cl bond length (Å)	2.5861(1) (eq)	2.5807(3) (eq)	2.6022(5) (eq)
	2.5808(1) (eq)	2.5943(4) (eq)	2.5977(5) (eq)
	2.5383(2) (eq)	2.5942(4) (eq)	2.5860(5) (eq)
	2.6105(3) (eq)	2.6348(4) (eq)	2.6587(5) (eq)
	2.4711(2) (ax)	2.4749(3) (ax)	2.4467(5) (ax)
	2.4717(2) (ax)	2.4628(3) (ax)	2.4637(5) (ax)
Mn-Cl-Mn angle (degrees)	178.474(7)	177.588(4)	176.191(3)
	173.637(5)	175.259(7)	177.344(5)

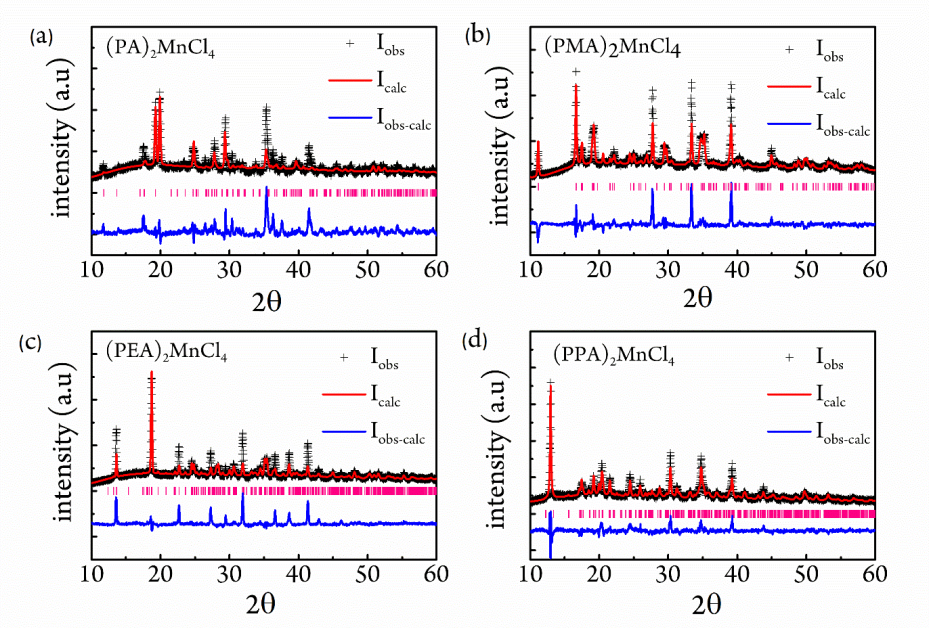

Figure 4.7 *Fits to powder XRD patterns of a) $(PA)_2MnCl_4$, b) $(PMA)_2MnCl_4$ c) $(PEA)_2MnCl_4$ and d) $(PPA)_2MnCl_4$ based on structural parameters determined by single-crystal XRD.*

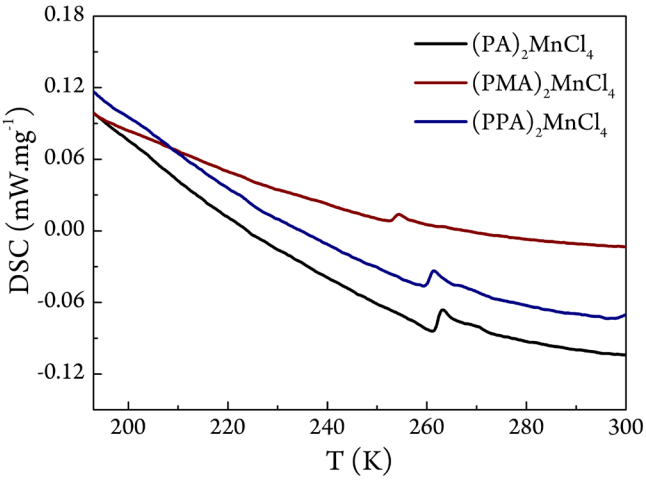

Figure 4.8 *DSC plots for $(PA)_2MnCl_4$, $(PMA)_2MnCl_4$ and $(PPA)_2MnCl_4$ over the range of temperature -80 to 30 °C. Peaks around 200K to -300K °C are most likely due to the presence of residual water in the purge gas used during measurement. No evidence of any structural phase transition accompanies these DSC peaks.*

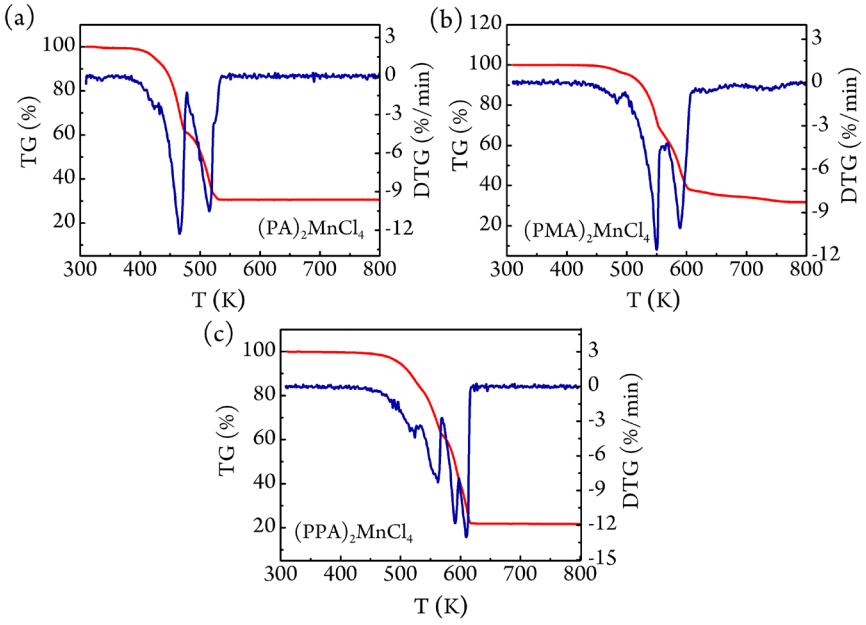

Figure 4.9 *TG/DTG plots for a) $(PA)_2MnCl_4$, b) $(PMA)_2MnCl_4$ and c) $(PPA)_2MnCl_4$ from room temperature to 800 K*